# Axi-symmetric Earth models and inner-core anisotropy

## Peter M. Shearer*, Kenneth M. Toy† & John A. Orcutt†

* Department of Earth Sciences, University of Cambridge, Bullard Laboratories, Madingley Road, Cambridge CB3 0EZ, UK
† Institute of Geophysics and Planetary Physics, Scripps Institution of Oceanography, University of California, San Diego, La Jolla, California 92093, USA

*Seismic waves passing through the middle of the Earth travel slightly faster in a N–S direction than in an E–W direction. A comparison of travel times for different P-wave phases shows that most of this anomaly is within the inner core, and that uniform anisotropy of the inner core is the most likely cause.*

BODY wave travel times as tabulated by the International Seismological Centre (ISC) are increasingly being used to formulate three-dimensional models of mantle[1,2], core–mantle boundary[3,4], and inner-core structure[5,6]. Despite sophisticated inversion techniques, these studies produce models that often do not agree, even at very low-order terms, in their spherical harmonic expansions. It is difficult to evaluate the relative accuracy of the different models, because they result from relatively complicated processing techniques, which typically involve both corrections (that is, ellipticity, station, upper- and lower-mantle structure, core–mantle boundary structure) and smoothing (namely, averaging residuals within cells, spherical harmonic expansions, stochastic filtering).

One of the most serious unresolved questions in these analyses concerns the origin of the large $C_{20}$ (spherical harmonic coefficient) anomaly. It is clear from PKIKP travel-time studies[5,6] and normal-mode splitting studies[7–9] that, on average, the Earth is slightly faster in a N–S direction than in an E–W direction for rays and modes that sample deep within the earth. For near-vertical PKIKP rays, this difference is about 2 s. This suggests the presence of an axi-symmetric $C_{20}$ term in the pattern of lateral heterogeneity in the Earth, but the exact depth of this anomaly is controversial. Ritzwoller et al.[7] place the anomaly in the lower mantle and outer core, Creager and Jordan[3] place it at the core–mantle boundary (CMB), whereas Morelli et al.[6] argue that it must be within the inner core and go on to suggest that inner-core anisotropy, rather than lateral heterogeneity, may be responsible. For all of these models, the $C_{20}$ term is much larger than any of the other aspherical terms. Thus the question of the depth of the $C_{20}$ anomaly must be resolved before comparisons of higher-order terms in the models will be meaningful.

Our analysis will focus on the key question of the depth of the $C_{20}$ anomaly. Accordingly, we will consider only axi-symmetric Earth models, examining patterns of travel-time residuals averaged over longitude, and then comparing these patterns with those predicted by the various models. We will generally attempt to remove as much as possible of the bias introduced by the uneven distributions of sources and receivers, and smooth the data in order to concentrate only on the low-order terms. Complicated inversion schemes will be minimized, with corrections applied to the data only if they significantly affect the results.

We will conclude that the data strongly indicate a $C_{20}$ anomaly within the inner core, and that inner-core anisotropy, rather than lateral heterogeneity, is the most probable cause. Our preferred anisotropy model is hexagonally symmetric with a fast N–S symmetry axis, and is approximately uniform throughout the inner core.

## Procedure

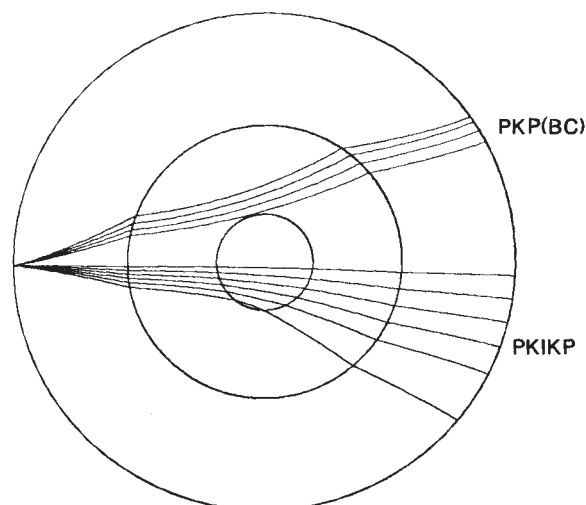A comparison of PKP(BC) and PKIKP residuals provides the



**Fig. 1** Ray paths for PKP(BC) and PKIKP phases.

most direct method of resolving the question of whether the $C_{20}$ anomaly exists within or outside the inner core. If the anomaly is within the inner core, then the PKIKP residuals should show a $C_{20}$ pattern, whereas the PKP residuals would not show this pattern. If the anomaly is outside the inner core (for example, at the core–mantle boundary), then both phases should show an anomalous pattern. The BC branch of PKP is most applicable for this comparison because it turns within the lowest part of the outer core. Figure 1 plots ray paths for PKP(BC) and PKIKP, and illustrates that the ray paths through the mantle and outer core are roughly the same for the two phases.

Figure 2a shows PKP(BC) travel-time residuals as a function of range for 174,028 PKP travel times (ISC 1964 to 1984). Residuals are calculated relative to the PR Earth model[10] and corrected for ellipticity. No station corrections or mantle model corrections are applied. The PR Earth model, as noted by Toy et al.[11], produces residuals with a mean of several seconds for deep body-wave phases. However, we are not concerned with radial Earth model deviations in this analysis, and so will only consider deviations from the mean residual. We attempt to minimize contamination from the AB and EF branches of PKP by using the relatively narrow four-second data window shown by the white lines in Fig. 2a. The turning-point radius for the BC branch of PKP varies from 1,221.5 km (the inner-core radius) to about 1,900 km. Figure 2b is a similar plot of 257,429 PKIKP travel-time residuals. As noted by Poupinet et al.[5], the arrivals are contaminated at ranges between 140° and 154° by the AB and BC branches and possible diffracted energy from the B caustic. We window the data as shown to remove this contamination; the missing data correspond to turning point radii of 905 to 1,155 km.
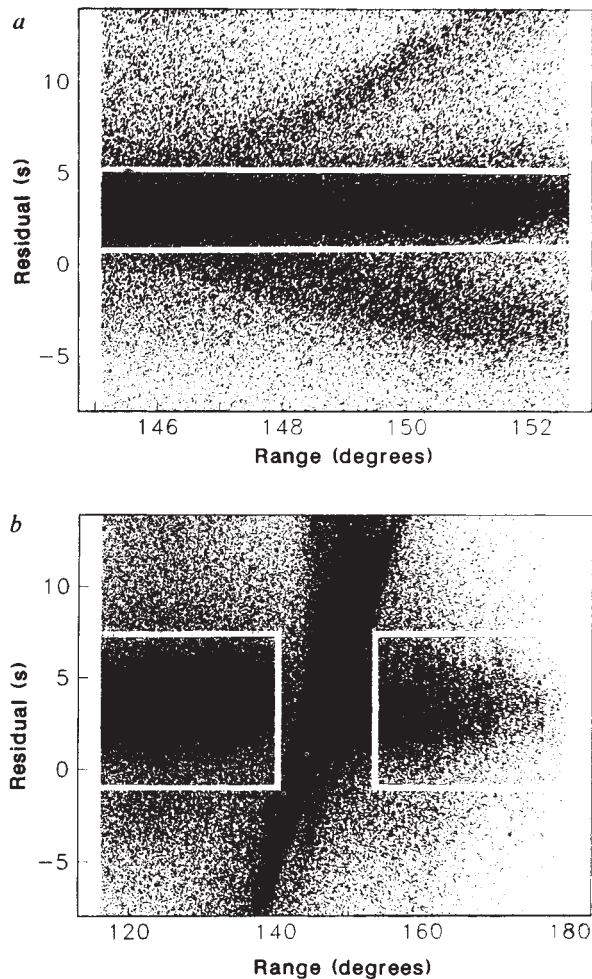
*a*

*b*

**Fig. 2** Travel-time residuals relative to the PR Earth model for: *a*, PKP(BC) arrivals, windowed as shown between 1 and 5 s in order to isolate the BC branch from the AB branch above and the EF branch below; *b*, PKIKP arrivals windowed as shown between −0.8 s and 7.2 s, excluding data between 140 and 150° which are contaminated by the AB and BC branches of PKP.

*a*

*b*

**Fig. 3** Axi-symmetric residuals for *a*, PKP(BC) and *b*, PKIKP plotted as a function of turning point colatitude and ray angle from the N–S axis. 100 km on the vertical scale is equivalent to a 3 s residual. Early arrivals are indicated by negative residuals, so, for example, a curve which is concave downward indicates faster arrivals at 0° and 180° than at 90°. The missing data between 900 and 1,150 km radius correspond to the contaminated region shown in Fig. 2*b*. Symbols indicate the number of 'independent' ray paths per data point, with squares indicating more than 200, triangles more than 50 and crosses more than 10. Data points with less than 4 paths are not plotted.

To show the axi-symmetric signal as a function of depth for these data, we plot the data in two different ways. First, we plot travel-time residuals versus the colatitude of the ray turning point. This type of plot is most sensitive to lateral heterogeneity at the turning point depth. Second, we plot the residuals versus the ray angle from the N–S axis at the turning point. This type of plot is most sensitive to hexagonally symmetric anisotropy of the type proposed for the inner core by Morelli *et al.*[6]. Changes in the shape of these residual curves with depth provide a direct method of resolving between inner-core anisotropy and lateral heterogeneity.

Because of the very uneven distribution of sources and receivers for the ISC data set, many studies have attempted to even out the data as much as possible by weighting observations from 'rare' ray paths proportionately more than data from 'common' ray paths. These averaging schemes typically take the form of dividing the data into bins which depend upon various parameters (such as source, receiver, or turning point location), and then averaging residuals within each bin, thus forming a reduced data set with a more uniform distribution than the complete data set. Assuming a reference radial Earth model and a given seismic phase, there are four independent parameters that completely describe the ray path. For example, the source and receiver locations (latitude and longitude) would specify the ray path. For our analysis, the turning-point depth and location, and the local ray angle at the turning point are the
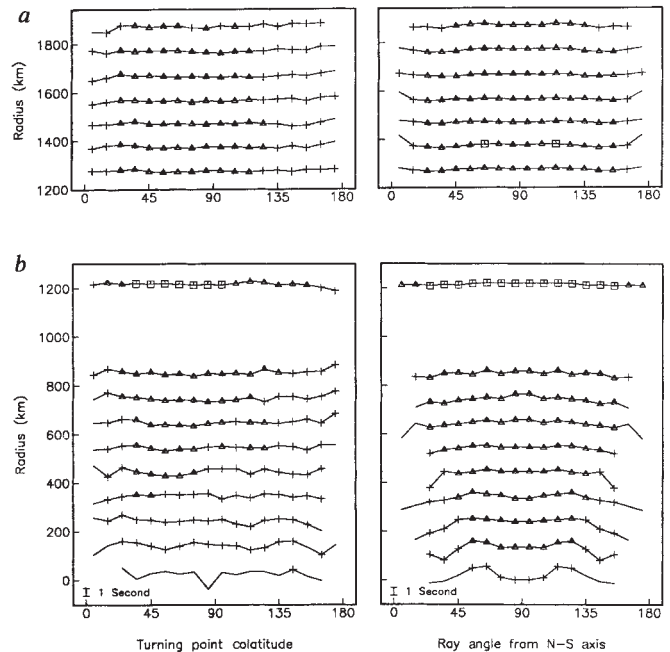
most important, and it is these four parameters that we use to sort and bin the data.

Our averaging scheme has the following form: first we divide the data by turning-point depth in intervals of 100 km. Second, we consider the turning-point latitude and longitude, and sort the data into 416 bins of roughly equal area, with a latitude spacing of 10° and a longitude spacing varying from 10° at the equator to 120° near the poles. Finally, within each bin, we further divide the data into 18 intervals of ray azimuth (measured from the local north on the surface of a reference sphere). Note that in general this ray azimuth differs from the ray angle from the N–S axis which we will eventually plot. The angles are related by $\theta = \cos^{-1} (\sin \phi \cos \omega)$, where $\theta$ is the ray angle from the N–S axis, $\phi$ is the colatitude of the turning point, and $\omega$ is the local ray azimuth. Because of the ray path reciprocity between sources and receivers, we consider local turning-point azimuths from 0° to 180° rather than from 0° to 360°. The averaging over longitude causes the ray-angle plots to be symmetric about $\theta = 90°$.

Thus, for each depth interval, we tabulate values for a 416 by 18 matrix, containing the average residual within each bin. This reduced data set forms the basis for the analysis which follows. Within the limitations of the finite number of bins, this sorting scheme is independent of the choice of coordinate axes. Because of the uneven distribution of sources and receivers, the matrix is very sparse, with only about 10% of the bins containing data. To plot travel-time residual versus turning-point colatitude, we simply average data from bins with the same colatitude. For the plots of residual versus ray angle from the N–S axis, we use the above equation to calculate this ray angle and then average all bins within 10° intervals. Each data point plotted in this paper is an average of from 4 to over 200 individual bins (see Fig. 3), where each bin represents a distinctly different ray path.
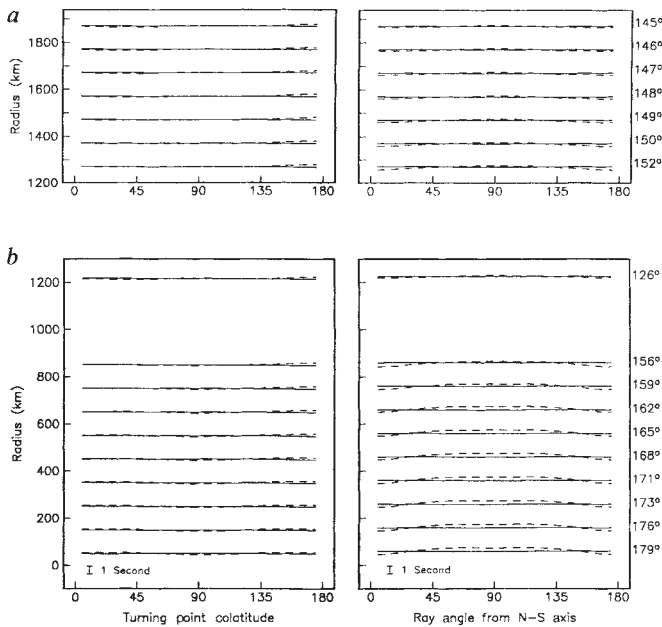
**Fig. 4** Axi-symmetric *a*, PKP(BC) and *b*, PKIKP residuals predicted by models of heterogeneity at the core–mantle boundary from Morelli and Dziewonski[4] (solid line) and Creager and Jordan[3] (dashed line), shown at intervals of 100 km in turning-point depth. Approximate ranges corresponding to these turning-point depths are shown at the right. 100 km on the vertical scale is equivalent to a 3 s residual.

Figure 3 shows these residual patterns as a function of turning-point depth. PKIKP data are missing at radii of 900 to 1,155, corresponding to the contaminated region shown in Fig. 2*b*. The uppermost PKIKP bin contains data at depths between 1,155 and 1,221.5 km (the inner-core radius), with most of the data in the top 10 km. The strongest anomaly pattern is visible in the ray-angle plot of PKIKP, with the polar arrivals fast compared to the equatorial arrivals, with this difference generally increasing with depth in the inner core. In contrast, the PKP(BC) residual plots show very little variation. This is direct evidence that most of the $C_{20}$ travel-time anomaly is probably within the inner core. The lack of a consistent pattern in the PKIKP turning-point colatitude plot indicates that the anomaly pattern is more compatible with inner-core anisotropy than with lateral heterogeneity.

## Model comparison

We compare these results with those predicted by several different models of the inner core and core–mantle boundary. These models include:

(1) The Morelli and Dziewonski[4] model of core–mantle boundary topography, derived from ISC PcP and PKP(BC) phases using a spherical harmonic expansion up to degree 4. Although the CMB varied by up to 6 km in this model, the axi-symmetric terms are very small ($C_{10} = 0.34$, $C_{20} = 0.14$, $C_{30} = -0.26$, $C_{40} = -0.11$ km).

(2) The Creager and Jordan[3] model of CMB heterogeneity derived from PKP(AB) and PKIKP phases. Axi-symmetric terms in the spherical harmonic expansion of their model are $C_{10} = -0.042$, $C_{20} = -0.104$, $C_{30} = 0.028$, $C_{40} = -0.048$, $C_{50} = -0.011$ s (Morelli and Dziewonski[4] normalization). These numbers represent the travel-time perturbation at the CMB for vertically travelling rays through core-side heterogeneity (their preferred model). A 0.1-s difference in vertical travel time at the CMB boundary is equivalent to about 2 km of CMB topography, so clearly this model is very different from the Morelli and Dziewonski model discussed above.
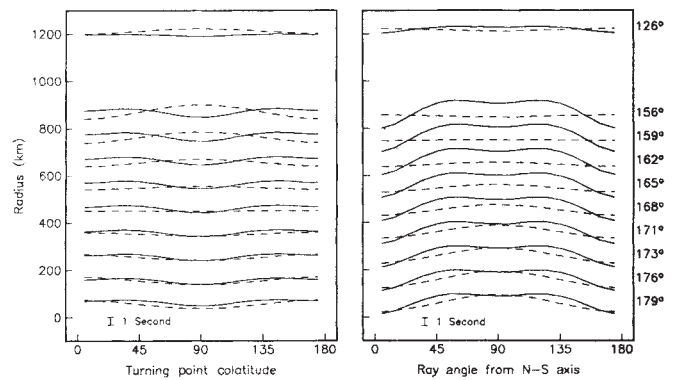


**Fig. 5** Axi-symmetric PKIKP residuals predicted by a model of inner-core anisotropy from Morelli *et al.*[6] (solid line) and an *ad hoc* of inner-core heterogeneity (dashed line). Scaling is as in Figs 3 and 4.

(3) The Morelli *et al.*[6] model of inner-core anisotropy. In this model, velocities in the inner core vary as

$$V = V_{eq}(1 + \varepsilon \cos^2 \theta + \sigma \cos^2 \theta \sin^2 \theta) \qquad (1)$$

where $V_{eq}$ is the equatorial velocity and $\theta$ is the ray angle from the N–S symmetry axis. This perturbation tapers with depth as $(r/R_{IC})^2$ in the inner core so that the model is isotropic at the centre of the Earth. Morelli *et al.* inverted near vertical PKIKP data (170–180° range) to obtain $\varepsilon = 0.032$ and $\sigma = -0.064$, numbers which imply a 3% difference in polar versus equatorial P-wave velocities near the surface of the inner core.

(4) A simple *ad hoc* model of inner-core heterogeneity. For this model, we assume a velocity perturbation in the inner core defined simply by a $C_{20}$ term which tapers with depth as $(r/R_{IC})^2$. At the surface of the inner core, $C_{20} = 0.1$ km s⁻¹, resulting in a model in which the inner core is fast near the poles and slow at the equator.

For vertical PKIKP rays, these models predict polar versus equatorial travel-time differences of $-0.03$, 0.88, 2.3 and 2.2 s, respectively. We calculate the effect of these models by tracing rays through the PR Earth model[10], rotating representative rays to different turning point positions and azimuths, summing along each path the residuals predicted by the models, and then averaging the residuals within the appropriate bins. The resulting residual patterns as a function of turning-point depth are shown in Figs 4 and 5.

The residuals predicted by the Morelli and Dziewonski[4] CMB model are barely noticeable at the scale of the plots (**Fig. 4**). The Creager and Jordan[3] CMB model predicts ray-angle residuals that appear to fit the more shallow turning PKIKP data (Fig. 3), but these residuals do not increase with depth to match the large PKIKP residuals deeper within the inner core. The Creager and Jordan model did not consider PKP(BC) data and was derived partially from PKIKP data, assuming inner-core homogeneity. The model predicts a PKIKP residual pattern similar in shape (but smaller by a factor of about 3) to that predicted by the Morelli *et al.*[6] model of inner-core anisotropy. If the Creager and Jordan model were increased in size to approximate the PKIKP residuals of the Morelli *et al.* model, the resulting PKP(BC) residuals would become too large to be consistent with the data. This indicates that most of the anomaly shown in the PKIKP data must be within the inner core, not at the core–mantle boundary. The relatively low-amplitude PKP(BC) residual pattern (Fig. 3) is roughly compatible with the pattern of both CMB models (Fig. 4). The Creager and Jordan model gives a somewhat better fit to the positive residuals at turning-point colatitudes near 180° and to the slightly concave-downward shape of the ray-angle residuals between 45° and 135°, whereas the Morelli and Dziewonski model gives a better
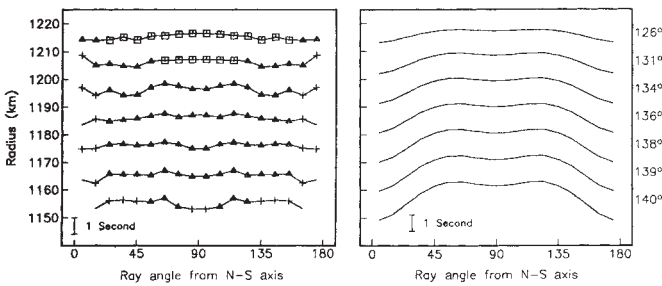
**Fig. 6** Ray angle residuals for shallow turning PKIKP rays, shown at intervals of 10 km in depth, compared with predicted results for the Morelli *et al.*[6] anisotropy model. Note the expanded time scale compared to the earlier plots; 1 s is equivalent to 6 km. Symbols are as in Fig. 3.

fit to the ray-angle data near the poles. But these PKP(BC) plots are most sensitive to anomalies at the turning-point depths (that is, in the lower part of the outer core), and are not ideal for comparing CMB structures. The relatively flat shape of the PKP(BC) ray-angle residual pattern argues against the recent hypothesis of anisotropy in the lower part of the outer core[12].

Figure 5 shows that the Morelli *et al.*[6] inner-core anisotropy model and our *ad hoc* heterogeneity model predict similar PKIKP residual patterns for the deepest turning rays. However, the predicted patterns diverge for the more shallow turning rays. For PKIKP rays turning at radii from 600 to 800 km, the $2\theta$ pattern in the ray-angle data is more consistent with the anisotropy model than the flat curve predicted by the heterogeneity model. The turning-point colatitude plots also favour the anisotropy model, with the concave-upward residual curves at radii of 600 to 800 km agreeing with the anisotropy model, but disagreeing sharply with the concave-downward curves predicted by the heterogeneity model. In addition, at deeper depths (radii from 100 to 300 km) the anisotropy model
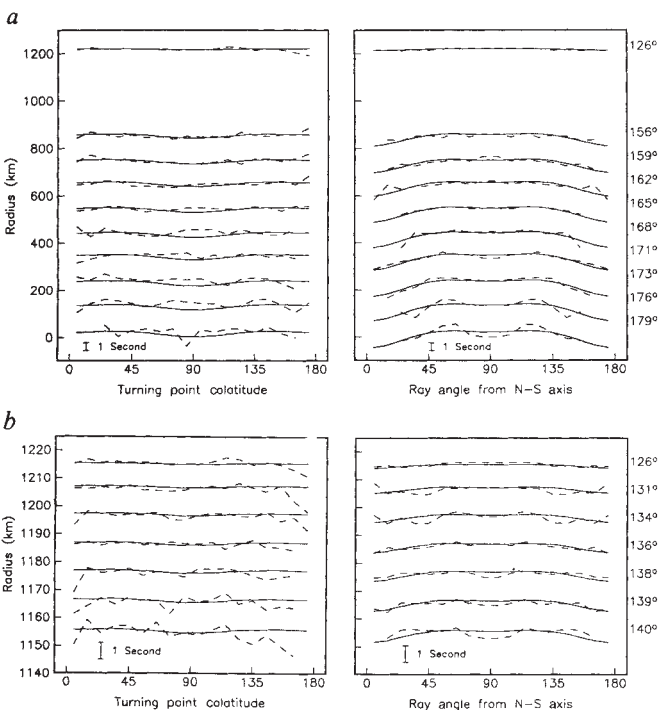
better reproduces the flattening in the residual curve near the equator.

The Morelli *et al.*[6] model, however, does not accurately predict the lessening of the ray-angle anomaly pattern with increasing radius in the inner core (compare Figs 3 and 5 at intermediate depths). This is because the $(r/R_{1C})^2$ factor in their model concentrates the anomaly near the surface of the inner core. Morelli *et al.*[6] preferred this model over a uniformly anisotropic inner-core model, because it agrees better with normal-mode splitting data[8], but our data show that such strong anisotropy near the surface of the inner core is incompatible with the PKIKP residual pattern for shallow turning rays.

This discrepancy can be seen most clearly if we examine the uppermost bin at 10 km intervals. Figure 6 is a close up of the top 70 km of the PKIKP residuals, showing a small but discernible $2\theta$ pattern in the ray-angle plots. Figure 6 also shows the predicted anomaly patterns for the Morelli *et al.* anisotropy model. Despite the shallow turning depths in the inner core, the model predicts very large residual anomalies, a result of the $(r/R_{1C})^2$ taper in the model concentrating the perturbations toward the surface of the inner core. The resulting residual patterns are clearly incompatible with the data.

## A uniform anisotropy model

A better fit to the PKIKP residual pattern can be obtained by assuming uniform anisotropy throughout the inner core. To obtain such a model, we consider velocity perturbations of the form

$$V = A + B \cos 2\theta + C \cos 4\theta \qquad (2)$$

where $\theta$ is the ray angle from the N-S symmetry axis. Note that this is equivalent to equation (1), where $A = V_{eq}(1 + \varepsilon/2 + \sigma/8)$, $B = V_{eq}\varepsilon/2$, $C = -V_{eq}\sigma/8$. When the anisotropy is weak ($B$, $C \ll A$), this expression is a good approximation to the equation first derived by Backus[13] and discussed extensively by Crampin[14]: $V^2 = A' + B' \cos 2\theta + C' \cos 4\theta$, where $A' = A^2$, $B' = 2AB$, $C' = 2AC$. Assuming a (001) hexagonal symmetry axis, we also have expressions for some of the elastic constants[13,14]: $\Gamma_{3333} = A' + B' + C'$, $\Gamma_{1111} = \Gamma_{2222} = A' - B' + C'$, $\Gamma_{1133} + 2\Gamma_{1313} = A' - 3C'$, where $\Gamma_{ijkl}$ is the density-normalized elastic tensor.

Using equation (2), we perform a simple least-squares fit to the PKIKP ray-angle data shown in Fig. 3, assuming no depth dependence for the anisotropy. The resulting values ($B = 0.054$, $C = 0.024$ km s$^{-1}$) are sufficient to reduce the variance of the ray-angle residuals by 68%. Predicted PKIKP residual curves for our model are compared with the data in Fig. 7a. The ray-angle fit is excellent at most depths, except for some mismatch near the endpoints (0 and 180°) and for the deepest turning rays (0-200 km radius). These are sparse areas of the data set, where we might expect the results to be somewhat noisier.

The predicted colatitude residual curves correspond less well to the data, but are still in reasonable agreement. Particularly encouraging is the reproduction of the slightly concave-upward shape of the residual curves at radii between 600 and 800 km. As a further test of our anisotropy model, we compare predicted residuals versus the data for the shallow turning PKIKP rays (see Fig. 7b). The ray-angle residual agreement is good at all depths, despite the fact that our inversion uses only the uppermost bin (1,210-1,221.5 km).

The agreement between our model and the data should not be exaggerated as the 68% variance reduction applies only to the binned and averaged data, not to the 257,429 individual PKIKP travel-time residuals, which are, of course, much noisier. The ray-angle plots are most sensitive to anisotropy, and exhibit the closest fit to the data. The colatitude plots fit less well, and indicate that some lateral heterogeneity may also be present in the inner core. In general, however, it is clear that the bulk of the axi-symmetric residual pattern can be fit with a uniform anisotropy model involving just two free parameters.



**Fig. 7** PKIKP residuals predicted by a simple model of uniform inner-core anisotropy (solid line), compared with the data (dashed line) for the entire inner core, *a*, and for the uppermost 70 km of the inner core, *b*. Scaling is as in Figs 3 and 7.

The relatively large size of the $4\theta$ term in our model (46% of the $2\theta$ term) is what causes the equatorial flattening in the ray-angle residual data curves shown in Fig. 7. The data also consistently exhibit this flattening, suggesting that a significant $4\theta$ term is a real feature of inner-core anisotropy. If inner-core anisotropy is a result of preferred crystal alignment (which seems the most probable cause), then the observed ratio of about 2 between the $2\theta$ and $4\theta$ coefficients may provide an important constraint on the crystal structure of the inner core.

Our anisotropy model ($B = 0.054$, $C = 0.025$ km s$^{-1}$) predicts anisotropic $P$-wave velocity variations of slightly under 1% at the surface of the inner core. In attempting to reconcile normal-mode splitting data with PKIKP travel-time data, Woodhouse et al.[8] noted that the anisotropy required at the surface of the inner core to explain the mode splitting is about a factor of two larger than the anisotropy indicated by the PKIKP residuals. This comparison assumed the Morelli et al.[6] PKIKP anisotropy

model, in which the anisotropic velocity variations are over 3% near the surface of the inner core. However, we have shown that such large velocity variations at these depths predict residual patterns which are incompatible with the PKIKP data for rays turning at shallow to intermediate depths within the inner core. Our preferred uniform model of inner core anisotropy is ~6 times too small to explain the normal-mode splitting data. Although we cannot rule out the possibility that a more complicated model of inner-core anisotropy and/or heterogeneity might still reconcile the PKIKP and normal-mode data sets, it seems unlikely that the primary source for the $C_{20}$ anomaly pattern in the normal-mode data is within the inner core. A key question for future research will be to resolve between the different models[3,4,7] which have been proposed for the core-mantle boundary to see if a single model can be found for this region which is compatible with both normal-mode and travel-time data.

1. Clayton, R. W. & Comer, R. P. Trans. Am. geophys. Un. 64, 776 (1983).
2. Dziewonski, A. M. J. geophys. Res. 89, 5929–5952 (1984).
3. Creager, K. C. & Jordan, T. H. Geophys. Res. Lett. 13, 1497–1500 (1986).
4. Morelli, A. & Dziewonski, A. M. Nature 325, 678–683 (1987).
5. Poupinet, G., Pillet, R. & Souriau, A. Nature 305, 204–206 (1983).
6. Morelli, A., Dziewonski, A. M. & Woodhouse, J. H. Geophys. Res. Lett. 13, 1545–1548 (1986).

7. Ritzwoller, M., Masters, G. & Gilbert, F. J. geophys. Res. 91, 10203–10228 (1986).
8. Woodhouse, J. H., Giardini, D. & Li, X.-D. Geophys. Res. Lett. 13, 1549–1552 (1986).
9. Giardini, D., Li, X.-D. & Woodhouse, J. H. Nature 325, 405–411 (1987).
10. Dziewonski, A. M. & Anderson, D. L. Phys. Earth planet. Inter. 25, 297–356 (1981).
11. Toy, K. M., Olson, A. H. & Orcutt, J. A. Trans. Am. geophys. Un. 67, 1099 (1986).
12. Gudmundsson, O., Clayton, R. W. & Anderson, D. L. Trans. Am. geophys. Un. 68, 1378 (1987).
13. Backus, G. E. J. geophys. Res. 70, 3429–3439 (1965).
14. Crampin, S. Geophys. J. R. astr. Soc. 49, 9–27 (1977).

# Crystal structure of an antifreeze polypeptide and its mechanistic implications

## D. S. C. Yang*, M. Sax*, A. Chakrabartty† & C. L. Hew†

* Biocrystallography Laboratory, VA Medical Center, PO Box 12055, Pittsburgh, Pensylvania 15240 and Department of Crystallography, University of Pittsburgh, Pittsburgh, Pennsylvania 15260, USA
† Research Institute, Hospital for Sick Children, Toronto and Departments of Biochemistry and Clinical Biochemistry, University of Toronto, Toronto M5G 1L5, Canada

*The X-ray crystallographic structure of an antifreeze polypeptide from the fish winter flounder, has been determined at 2.5 Å by an analysis of the Patterson function. This is the first report of a polypeptide of this size that is a single α-helix. A proposed mechanism of antifreeze binding to ice surfaces is given which requires: first, that the dipole moment from the helical structure dictates the preferential alignment of the peptide to the c-axis of ice nuclei; second, amphiphilicity of the helix; and third, torsional freedom of the side chains to facilitate hydrogen bonding to ice surfaces.*

FREEZING is lethal to most cellular organisms. Dehydration of the intracellular environment and physical damage by ice crystals are the major causes for freezing injury and death. Many marine fishes living in cold, polar waters survive in the ice-laden surroundings by synthesizing a unique class of serum proteins which prevent their blood sera from freezing. Aqueous solutions containing these proteins, commonly known as antifreeze proteins, possess many unusual freezing properties[1–3].

Isolation and subsequent characterization of these proteins from different fishes have established the diversity of their chemical structures. At least one type of antifreeze glycoprotein (AFGP) and three types of antifreeze polypeptides (AFP) are known. All the AFGPs isolated so far are similar in chemical structure. They are polymers of a glycotripeptide unit, Ala Ala Thr, with a disaccharide linked to the Thr side chain. The AFPs, on the other hand, are quite diverse structurally. They can be grouped into three classes, namely, the alanine-rich AFPs, cysteine-rich AFPs and a third class that is neither rich in alanine nor cysteine[4].

The properties of antifreeze proteins have been investigated using a number of techniques including freezing point osmometry, $^{13}$C-NMR, electron microscopy, Raman spectroscopy, light scattering and so on[3,5]. All AFGPs and AFPs appear

to operate via a noncolligative mechanism and depress freezing temperature to a greater extent than the melting temperature. On a weight basis they are as efficient as salt (NaCl) in lowering the freezing temperature, but on a molar basis they are 300–500-fold more efficient.

We report here the first crystallographic analysis of the three dimensional structure of an antifreeze polypeptide molecule. The initial phase determination was based on an analysis of the Patterson function, therefore, it is also the first report of a structure of this size that was essentially determined by the Patterson method. The antifreeze molecule is a single α-helix. Based on the well established dipolar character of α-helix[6,7], a mechanism has been put forth to explain the specific binding of antifreeze molecules to the prism faces (defined as faces parallel to the c-axis) of the ice nuclei.

## Alanine-rich AFPs

This class of AFP is the most extensively characterized. Those that have been studied were isolated from fish from two different phylogenetic families; the winter flounder of the right eye flounder family, and the shorthorn, arctic and grubby sculpins of the cottid family[8–10]. The amino-acid sequences of these AFPs are shown in Table 1. The structural characteristics of these AFPs